Article

Journal of Vibration and Control
2021, Vol. 0(0) 1–18

DOI: 10.1177/10775463211019177
journals.sagepub.com/home/jvc

Implementation and intelligent gain tuning feedback–based optimal torque control of a rotary parallel robot

Farzam Tajdari[1] and Naeim Ebrahimi Toulkani[2]

Abstract

Aiming at operating optimally minimizing error of tracking and designing control effort, this study presents a novel generalizable methodology of an optimal torque control for a 6-degree-of-freedom Stewart platform with rotary actuators. In the proposed approach, a linear quadratic integral regulator with the least sensitivity to controller parameter choices is designed, associated with an online artificial neural network gain tuning. The nonlinear system is implemented in ADAMS, and the controller is formulated in MATLAB to minimize the real-time tracking error robustly. To validate the controller performance, MATLAB and ADAMS are linked together and the performance of the controller on the simulated system is validated as real time. Practically, the Stewart robot is fabricated and the proposed controller is implemented. The method is assessed by simulation experiments, exhibiting the viability of the developed methodology and highlighting an improvement of 45% averagely, from the optimum and zero-error convergence points of view. Consequently, the experiment results allow demonstrating the robustness of the controller method, in the presence of the motor torque saturation, the uncertainties, and unknown disturbances such as intrinsic properties of the real test bed.

Keywords

Stewart platform, optimal torque control, validation, nonlinear system, robustness

1. Introduction

In applications where higher acceleration and velocity and better accuracy and lighter weight are essential or where a comparatively high bearing capacity per robot weight is required, parallel mechanisms are alternatively preferred to serial manipulators (Taghirad 2013, Tajdari et al. 2017b). Namely, some of the applications are space interferometry, spacecraft communication devices (Furqan et al., 2017), flight simulator (Huang et al., 2016), surgery (Orekhov et al., 2016) production line, and scanning (Huang et al., 2018). Among the other things, the high accuracy scanning of the human body for the purpose of surgeries, designing anatomical adaptable rehabilitation devices (Nomura et al., 2016), and next generation of Ultra Personalized Products and Services (UPPS) (Kwon and Kim 2012, Yang et al. 2020) attract more attention. It shows the importance of health and humanity survival and how it is influenced by robots' high precision. One of the interesting scanning scenarios is fast automated breast scanning (Chen et al. 2015, Merouche et al. 2015, Sun et al. 2018) which is supposed as the future application of this study. However, because of the flexibility and deformation of the breast tissue, it is a very complex action. The needs of such robots are revealed especially during motion scanning.

High accuracy needs good knowledge of kinematic, dynamic, and control of a parallel robot to investigate complex dynamic and accordingly sophisticated control approaches (Shoham et al., 2003). Well-known parallel robots with wide usage in the aforementioned applications were extracted from the mechanism presented by Gough (1962) and Stewart (1965) based on the fundamental of the recent parallel robots.

Addressing the first issue, solving the kinematics of the parallel robots is considerably complicated because they do not have a definite solution. Also, there is no closed form for these kinds of equations (Sosa-Méndez et al., 2017). Kinematics of the robot with linear manipulator was widely studied in recent years, namely Geng et al. (1992); Petrescu et al. (2018); and Tajdari et al. (2020c), whereas

[1]Faculty of Industrial Design Engineering, TUDelft, Netherlands
[2]Aerospace Engineering, Sharif University of Technology, Iran

Received: 1 September 2020; accepted: 1 May 2021

Corresponding author:
Farzam Tajdari, Faculty of Industrial Design Engineering, Delft University of Technology, Landbergstraat 15, Delft 2628 CE, Netherlands.
Email: f.tajdari@tudelft.nl

mechanisms with rotary actuators are less studied due to additional complexity of rotation. Thus, in this article, a Stewart robot with rotary manipulator is investigated, owing to the fact that it is faster than a Stewart platform with linear actuators in control responses (Van Nguyen and Ha, 2018). Also, it has less production and maintenance cost, less weight, easier installation procedure (e.g., surgical goals), and powerful ability of integration with other mechanisms (Patel et al., 2018).

Regarding the complex mechanism, the kinematic equation of the robot is a key to dynamical analysis of the parallel robot. In addition, main challenges in the deriving of the dynamic equations are the relationship description between internal or external forces and torques, the states of end effector for controller design, and feasibility study of the robot. Considering the dynamical analysis, several approaches were used such as the comprehensive approach based on momentum (Lopes, 2009), the Newton–Euler methodology (Dasgupta and Mruthyunjaya, 1998), and the Lagrangian approach (Bingul and Karahan, 2012). Furthermore, based on the assumptions for using either of the approaches, different solutions were proposed. One of the solutions assumed dynamic simplifications to the robot such as ignoring friction joints in the links and concluding a basic legs dynamic Do and Yang (1988), Fichter (1986), Merlet (1990), Sugimoto (1989). Some other studies, such as Dasgupta and Mruthyunjaya, 1998), developed a generalized model according to the Newton–Euler formulation to study the effectiveness of the viscous friction in the joints. Also, the Lagrange formulation was used in Lebret et al. (1993).

To assess the automation and the equation of motions, and because there are nonlinearity and uncertainty in the fabricated robot, a computing software capable of simulating inverse kinematic, dynamic motion, and state variable is necessary. To this end, ADAMS is used in this study. The aforementioned software was also used in Cafolla and Marco (2015), Gough (1957), and Stewart (1965). Accordingly, a proper ADAMS model is used in the current article based on the proposed model in Tajdari et al. (2020b). This model is capable to verify any controller approach for the rotary robot dynamic.

The main objective of controller design in parallel robots is to move end effector of the robot precisely, so that it can follow a desired trajectory and orientation of dynamic or static variables (Merlet, 2006). There are many control schemes, which are based on the models and applicable for linear manipulator Stewart robots, namely optimal feedback linearization control (Tajdari et al. 2021a; Tourajizadeh et al. 2016), control of inverse dynamic (Lee et al., 2003), backstepping tracking adaptive control (Huang and Fu, 2004), sliding mode, and PID controllers (Kizir and Bingul 2012; Tajdari et al. 2017a), whereas there are less control approaches for a rotary Stewart robot due to the additional complexity of the robot's dynamic. Moreover, in the most of the latter methods, controlling the length of links in the robots was used to control the states of the end effector. As a result, a comprehensive methodology for direct controlling from manipulators to the end effector was missed. Consequently, using the position control methodology solely limits the robot design to the joint space (Hopkins and Williams, 2002). In particular, the control methodologies based on the inverse dynamic are substantial to control the end effector motion through the manipulators, directly. Then, there is the possibility of investigating experimental constraints, for example, manipulator saturation, and uncertainty considerations. However, there are limited studies discussing the rotary robot torque control.

Thus, this article aims to develop and test a novel integral torque control methodology for the complicated parallel mechanism to optimize the torques and minimize the tracking error. This is an opening for further implementation of identification approaches, nonlinear control methods, and impedance manipulator control (Yang et al., 2019). The scientific contributions of this article are as follows:

1. Introducing the design architecture of the robust integral controller integrated with an anti-windup scheme, which solves unknown disturbances and manipulator saturation;
2. Integrating an intelligent optimizer gain tuner in the metric for establishing a robust optimal controller with faster zero-error convergence performance;
3. Extensively investigating the sensitivity level, robustness, and attraction region of the controller parameters, and demonstrating the global stability of the controller, which guarantees the global zero-error convergence; and
4. Implementing the controller on a reliable nonlinear system, via ADAMS to validate the robustness, and convergence in different scenarios and also on a fabricated Stewart robot to assess the performance in presence of naturalistic disturbance, manipulators' saturation, and uncertainties.

An introductory version of this study was presented in Tajdari et al. (2020b), which is collaborated here with a more rigorous concept; a comprehensive demonstration on stability of controller properties for the suggested control law; investigation on level of robustness with respect to parameter choices through numerical experiments; and additional numerical experiments, containing a scenario which presents a state-of-the-art conventional control methodology and a scenario, which includes additional disturbances through the fabricated robot.

2. Stewart platform: Dynamical equations

To derive the equations of motion of a Stewart mechanism, kinematics and kinetics analyses of the dynamical system

are required. This step is crucial toward obtaining the relationships between the position and the velocity of the end effector before dynamic analysis.

2.1. Kinematics equation

In a Stewart platform which is actuated with rotary motors, controllable variables are the output torques of motors and their rotational angels. In the following equations, a relationship between the motors' variables and the position of the end effector is presented

$$\overline{X} = \begin{bmatrix} \phi \\ \theta \\ \psi \\ x \\ y \\ z \end{bmatrix}, \quad \overline{L} = \begin{bmatrix} L_1 \\ L_2 \\ L_3 \\ L_4 \\ L_5 \\ L_6 \end{bmatrix} = f(\overline{X}), \quad \theta_M = \begin{bmatrix} \theta_{M_1} \\ \theta_{M_2} \\ \theta_{M_3} \\ \theta_{M_4} \\ \theta_{M_5} \\ \theta_{M_6} \end{bmatrix} = g(\overline{L}) \tag{1}$$

Vector $\overline{X}$ represents the end effector's variables which are the rotation angles ϕ, ψ, and θ of the moving plate about the X, Y, and Z axis, respectively, and the position of the end effector center of mass as x, y, and z with respect to the fixed coordinate XYZ. Moreover, the vector $\overline{L}$ refers to the distance between the joints on the fixed base ($\overrightarrow{P}_i$) and the corresponding joints on the movable frame ($\overrightarrow{p}_i$). Eventually, θ_M is the motor angular shown in Figure 1(a). The connecting vector from $\overrightarrow{P}_i$ to $\overrightarrow{p}_i$ can be written as

$$\overrightarrow{L}_i = \left(R_{xyz}^{-1}\overrightarrow{p}_i + G\right) - \overrightarrow{P}_i = f(\overline{X}) \tag{2}$$

where

$$R_{xyz} = R_x(\phi)R_y(\theta)R_z(\psi) = \begin{bmatrix} C\phi C\psi & C\theta S\psi & -S\theta \\ C\psi S\theta S\phi - C\phi S\psi & C\phi C\psi + S\theta S\phi S\psi & C\theta S\phi \\ C\theta C\psi S\theta + S\phi S\psi & C\phi S\theta S\psi - c\psi S\phi & C\theta C\phi \end{bmatrix} \tag{3}$$

considering the fact that $C\theta_x = \mathrm{Cos}(\theta_x)$, $S\theta_x = \mathrm{Sin}(\theta_x)$. And, G, position vector of the end effector center of mass, is determined as

$$G = [x, y, z]^T \tag{4}$$

Considering the length of each legs in equation (2), the length of each link connecting the end effector to the base is written as

$$\left|\overrightarrow{l_i}\right| = \left|R_{xyz}^{-1}(\overrightarrow{p}_i + G) - \left(\overrightarrow{P}_i + \overrightarrow{u}_i\right)\right| \tag{5}$$

where $\overrightarrow{u}_i$ is the vector representing the link connected to the motor. The vector is shown in Figure 1(a) and calculated as follows

$$\overrightarrow{u}_i = |\overrightarrow{u}_i|R_z(\theta_h)\mathrm{Sin}(\theta_M)\mathrm{Cos}(\beta)\overrightarrow{i} + \mathrm{Cos}(\theta_M)\overrightarrow{j} + \mathrm{Sin}(\theta_M)\mathrm{Sin}(\beta)\overrightarrow{k} \tag{6}$$

where θ_h is the angle between $\overrightarrow{P}_i$ and $\overrightarrow{X}$ in global axis, and β is the installation angle between the motor and the horizon. Thus, by replacing equation (6) with equation (5), and considering that length $\overrightarrow{l}_i$ is always constant, θ_{M_i} can be extracted as

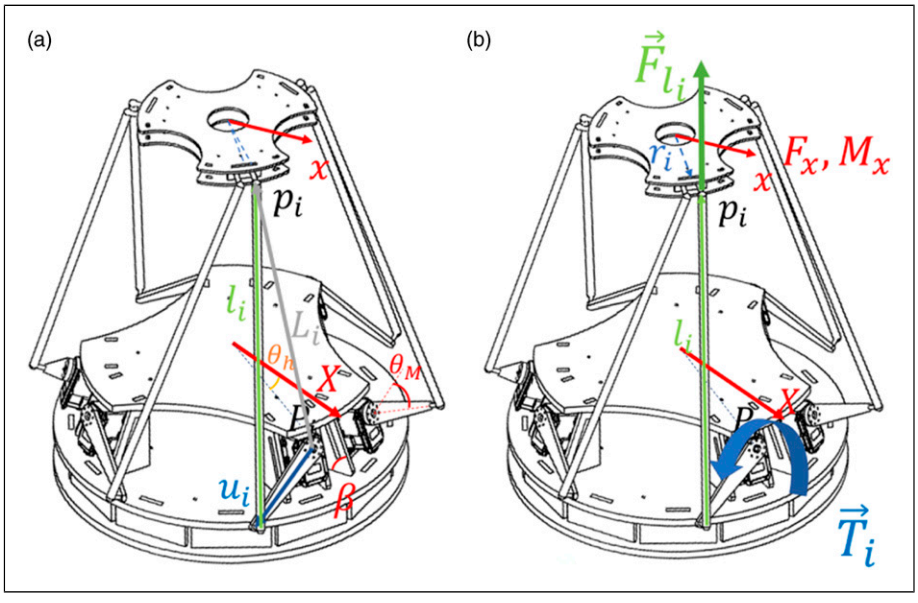

Figure 1. Schematic of a Stewart platform. (a) Defined variables and vectors. (b) Dynamic force–torque diagram.

$$\theta_{M_i} = -\left(a\sin d\left(\frac{\mathcal{C}_i}{\sqrt{\mathcal{A}_i^2 + \mathcal{B}_i^2}} \right) - a\cos d\left(\frac{\mathcal{B}_i}{\sqrt{\mathcal{B}_i^2 + \mathcal{A}_i^2}} \right) + 180 \right) \tag{7}$$

where $\mathcal{A}_i, \mathcal{B}_i, \mathcal{C}_i \in U(\overline{X})$

$$\mathcal{A}_i = 2|\overrightarrow{u}_i|\left(\left|\overrightarrow{L}_{i_x}\right|\mathrm{Sin}(\theta_h) - \left|\overrightarrow{L}_{i_y}\right|\mathrm{Cos}(\theta_h) \right) \tag{8}$$

$$\mathcal{B}_i = 2|\overrightarrow{u}_i|\left|\overrightarrow{L}_{i_x}\right|\mathrm{Cos}(\beta)\mathrm{Cos}(\theta_h) + \left|\overrightarrow{L}_{i_y}\right|\mathrm{Cos}(\beta)\mathrm{Sin}(\theta_h) - \left|\overrightarrow{L}_{i_z}\right|\mathrm{Sin}(\beta) \tag{9}$$

$$\mathcal{C}_i = \left|\overrightarrow{l}_i\right|^2 - \left|\overrightarrow{L}_i\right|^2 \tag{10}$$

Equation (7) defines that practically having the $\overline{X}$ through a sensor on the end effector leads to have the angle value of each motor. This is helpful for position control of these kinds of robots.

2.2. Kinetics equations

In this section, the dynamical equations of a Stewart platform actuated by six rotary motors are obtained using the Newton–Euler method. The derivations are summarized just to show different dynamic features of the systems and the effects. Figure 1(a) shows a Stewart mechanism with six rotary motors as actuators. As it can be seen, the platform consists of a moving plate as the end effector, a fixed plate as the base, and six legs connected to six rotary actuators, as the manipulators to move the end effector. The spherical joints are used to connect the six legs, the end effector, and the base. The kinetics equations for the end effector can be written as

$$\Sigma\overrightarrow{M} = \overline{I}\,\overrightarrow{\alpha} \tag{11}$$

$$\Sigma\overrightarrow{F} = \overline{m}\,\overrightarrow{a} \tag{12}$$

$$\begin{bmatrix} \overline{I} & 0_{3\times3} \\ 0_{3\times3} & \overline{m} \end{bmatrix} \begin{bmatrix} \ddot{\phi} \\ \ddot{\theta} \\ \ddot{\psi} \\ \ddot{x} \\ \ddot{y} \\ \ddot{z} \end{bmatrix} = \begin{bmatrix} M \\ F \end{bmatrix} \tag{13}$$

where $\overrightarrow{\alpha}$ is the angular acceleration vector and $\overrightarrow{a}$ is the linear acceleration vector of the end effector. In addition, $\overline{m}$ contains the mass value (m) of the end effector and $\overline{I}$ defines the end effector moment of inertia around x, y, and z axis, denoted as

$$\overline{I} = \begin{bmatrix} I_{xx} & 0 & 0 \\ 0 & I_{yy} & 0 \\ 0 & 0 & I_{zz} \end{bmatrix}, \quad \overline{m} = \begin{bmatrix} m & 0 & 0 \\ 0 & m & 0 \\ 0 & 0 & m \end{bmatrix} \tag{14}$$

and

$$M = [M_x, M_y, M_z]^T, \quad F = [F_x, F_y, F_z]^T \tag{15}$$

In Figure 1(b), M and F represent the torques and the exerted forces on the end effector, respectively. Addressing the rotary motors' manipulated torques, the dynamic equation should be derived as a controllable variable–torque relationship discussed in the following

$$\begin{bmatrix} \overline{I} & 0_{3\times3} \\ 0_{3\times3} & \overline{m} \end{bmatrix} \begin{bmatrix} \ddot{\phi} \\ \ddot{\theta} \\ \ddot{\psi} \\ \ddot{x} \\ \ddot{y} \\ \ddot{z} \end{bmatrix} = \begin{bmatrix} M \\ F \end{bmatrix} = \tau_{6\times6} \begin{bmatrix} T_1 \\ T_2 \\ T_3 \\ T_4 \\ T_5 \\ T_6 \end{bmatrix} \tag{16}$$

where T_i is the manipulated torque with motor i. The kinetics equations can also be formed by using their unit vectors. It can be written as

$$\Sigma\overrightarrow{M} = \Sigma\overrightarrow{r}_i \times \overrightarrow{F}_{l_i} = \Sigma\overrightarrow{p}_i \times \overrightarrow{e}_{l_i}\left|\overrightarrow{F}_{l_i}\right| = \Sigma\overrightarrow{e}_{M_i}\left|\overrightarrow{F}_{l_i}\right| \tag{17}$$

where $\overrightarrow{e}_{M_i} = \overrightarrow{p}_i \times \overrightarrow{e}_{l_i}$, that is, $\overrightarrow{e}$ denotes the unit vector of its corresponding vector. Then

$$\Sigma\overrightarrow{F} = \Sigma\overrightarrow{e}_{l_i}\left|\overrightarrow{F}_{l_i}\right| \tag{18}$$

Thus

$$\begin{bmatrix} M \\ F \end{bmatrix} = \begin{bmatrix} e_{M_1} & \cdots & e_{M_6} \\ e_{l_1} & \cdots & e_{l_6} \end{bmatrix} \begin{bmatrix} F_{l_1} \\ \vdots \\ F_{l_6} \end{bmatrix} \tag{19}$$

where

$$\tau_1 = \begin{bmatrix} e_{M_1} & \cdots & e_{M_6} \\ e_{l_1} & \cdots & e_{l_6} \end{bmatrix} \tag{20}$$

As $\overrightarrow{F}_{l_i} = \overrightarrow{e}_{l_i} \cdot \overrightarrow{e}_{N_i}|\overrightarrow{T}_i|/|\overrightarrow{u}_i|$, where $\overrightarrow{e}_{N_i}$ is the unit vector of $\overrightarrow{T}_i$, therefore

$$\begin{bmatrix} F_{l_1} \\ \vdots \\ F_{l_6} \end{bmatrix} = \begin{bmatrix} \frac{\overrightarrow{e}_{l_1} \cdot \overrightarrow{e}_{N_1}}{|\overrightarrow{u}_1|} & \cdots & 0 \\ \vdots & \ddots & \vdots \\ 0 & \cdots & \frac{\overrightarrow{e}_{l_6} \cdot \overrightarrow{e}_{N_6}}{|\overrightarrow{u}_6|} \end{bmatrix} \begin{bmatrix} T_1 \\ \vdots \\ T_6 \end{bmatrix} \tag{21}$$

Considering

$$\tau_2 = \begin{bmatrix} \frac{\vec{e}_{l_1} \cdot \vec{e}_{N_1}}{|\vec{u}_1|} & \cdots & 0 \\ \vdots & \ddots & \vdots \\ 0 & \cdots & \frac{\vec{e}_{l_6} \cdot \vec{e}_{N_6}}{|\vec{u}_6|} \end{bmatrix} \tag{22}$$

the equation of motion would be

$$\begin{bmatrix} \overline{I} & 0_{3\times3} \\ 0_{3\times3} & \overline{m} \end{bmatrix} \begin{bmatrix} \ddot{\phi} \\ \ddot{\theta} \\ \ddot{\psi} \\ \ddot{x} \\ \ddot{y} \\ \ddot{z} \end{bmatrix} = \begin{bmatrix} M \\ F \end{bmatrix} = \tau_{6\times6} \begin{bmatrix} T_1 \\ T_2 \\ T_3 \\ T_4 \\ T_5 \\ T_6 \end{bmatrix} = \tau_1\tau_2 \begin{bmatrix} T_1 \\ T_2 \\ T_3 \\ T_4 \\ T_5 \\ T_6 \end{bmatrix} \tag{23}$$

Thus, the ultimate dynamic transfer matrix, from the end effector to the base, can be obtained as

$$\tau = \begin{bmatrix} e_{M_1} & \cdots & e_{M_6} \\ e_{l_1} & \cdots & e_{l_6} \end{bmatrix} \begin{bmatrix} \frac{\vec{e}_{l_1} \cdot \vec{e}_{N_1}}{|\vec{u}_1|} & \cdots & 0 \\ \vdots & \ddots & \vdots \\ 0 & \cdots & \frac{\vec{e}_{l_6} \cdot \vec{e}_{N_6}}{|\vec{u}_6|} \end{bmatrix} \tag{24}$$

where τ is a transfer matrix that defines the equations of motion based on the end effector states and the applied torques by the actuators. It provides suitable circumstance to implement the torque control method, directly, and is shown as below

$$\ddot{\overline{X}} = \tau_{tot} T \tag{25}$$

where

$$\tau_{tot} = \begin{bmatrix} \overline{I} & 0_{3\times3} \\ 0_{3\times3} & \overline{m} \end{bmatrix}^{-1} \tau \tag{26}$$

2.3. Evaluation of equations of motion and derivation of the nonlinear model

Providing a valid nonlinear model, which is able to represent the actual system, is crucial for the controller design and evaluation process. Some physical constraints such as collision of objects, hardness and elasticity of rigid bodies, and friction between hard surfaces could not be addressed in MATLAB. Therefore, ADAMS is used to simulate the Stewart model. However, lacking the capability of coding and implementation of different control methods in ADAMS makes it an insufficient tool for evaluating the system. To overcome this problem, MATLAB and ADAMS are connected together to implement the online control method on MATLAB and evaluate the controller performance on the nonlinear system modeled in ADAMS.

First, the 3D model of the system is designed in SolidWorks (Figures 2 (a) and (b))). Next, the 3D model is imported into the ADAMS and then the essential constraints such as joint types, materials and densities of the bodies, rigidity of them toward each other, and frictions between hard surfaces are applied to the modeled robot. Tables 2 and 1 show the considered values and assumptions for the design variables. As it is reported in Table 2, the system consists of 14 components of mass and moment of inertia. Figure 2(c) shows all the applied constraints to the 3D

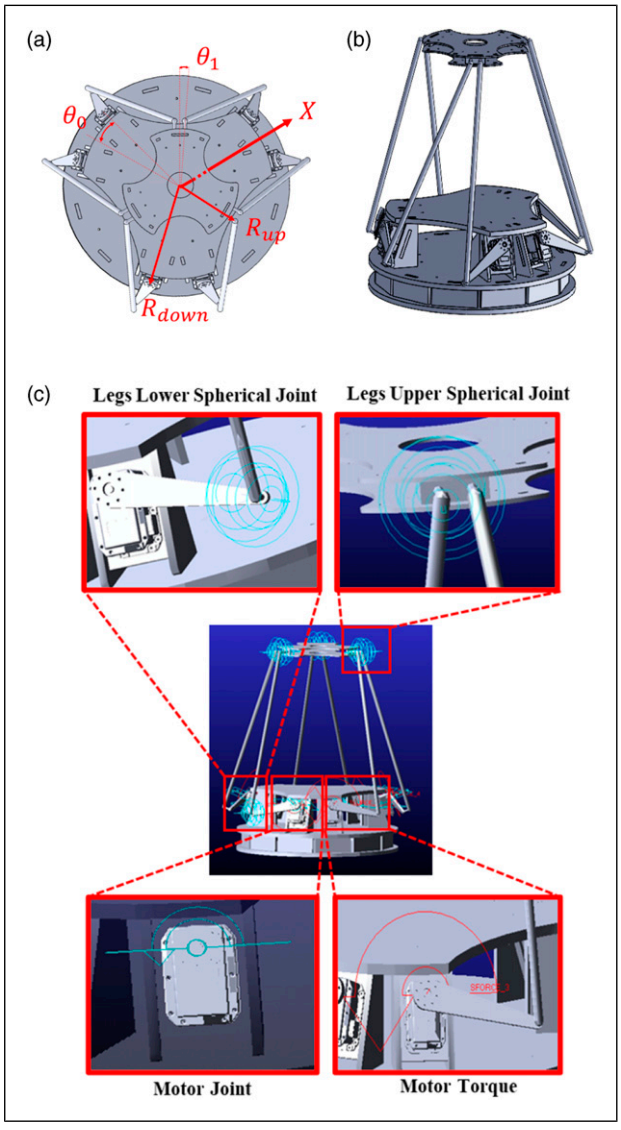

Figure 2. 3D model of the Stewart platform. (a) In SolidWorks top view. (b) In SolidWorks perspective view. (c) In ADAMS with the applied constraints.

model. As shown, a bidirectional torque, represented by red vectors, is applied on each leg.

3. Controller design

According to the fact that the designed dynamical system in ADAMS consists of nonlinear parameters of an actual system, it is definitely a nonlinear Stewart platform. Hence, to control these kinds of systems, the proposed controller needs to be capable of reducing the tracking errors in the presence of nonlinearities (Åström and Hägglund, 1995). In addition to robustness, optimization of the input signals in parallel manipulators to achieve an efficient performance is a challenge. The issue needs to be addressed in the controller design process. Therefore, a linear quadratic integral (LQI) optimal controller is an appropriate option to control the nonlinear system effectively.

3.1. State-space equations

The state space and dynamic equations of the Stewart robot can be formulated as follows

$$\dot{\bar{x}} = \overline{A}_c\bar{x}(t) + \overline{B}_c(t)T(t) + \overline{d}_c(t) \tag{27}$$

where $\bar{x}$ consists of the main states in $\overline{X}$, and the speed of the states. Consequently, the dynamic of the error can be defined as

Table 1. The choice of options.

Parameter	Value	Description
R_{up}	0.12 (m)	Length p_i
R_{down}	0.22 (m)	Length P_i
θ_0	5°	Angle joint on base
θ_1	15°	Angle joint on end effector
β	70°	The motor installing angle

$$\dot{\bar{e}} = \overline{A}_c\bar{e}(t) + \overline{B}_c(t)T(t) + \overline{d}_c(t) \tag{28}$$

which is discretized as

$$\bar{e}(k+1) = \left(I + \Delta t\overline{A}_c\right)\bar{e}(k) + \Delta t\overline{B}_c(k)T(k) + \Delta t\overline{d}_c(k) \tag{29}$$

where Δt is the time step. Considering $\overline{A} = I + \Delta t\overline{A}_c$, $\overline{B} = \Delta t\overline{B}_c$, and $\overline{d} = \Delta t\overline{d}_c$, then

$$\bar{e}(k+1) = \overline{A}\bar{e}(k) + \overline{B}(k)T(k) + \overline{d}(k) \tag{30}$$

where matrix T includes the manipulated torques and vector $\overline{d}$ represents the time-variant disturbances. $\bar{e}$ is the error matrix of the states and is defined as $\bar{e} = \bar{x} - x_d$, where x_d denotes the desired values of the states. Matrix $\overline{A}$ includes all the $a_{i,j}$ elements in equation (31) which represent the system dynamics. Finally, matrix $\overline{B}$ includes $b_{i,j}$ elements in equation (32) which represent the interconnections between the applied torques and corresponding states

$$a_{i,j} = \begin{cases} 1 & \text{if } i = j \\ \Delta t & \text{if } i = 2n-1, \quad \text{and} \quad j = i+1 \\ 0 & \text{otherwise} \end{cases} \tag{31}$$

$$b_{i,j} = \begin{cases} \Delta t\,\tau_{tot}\left(\frac{i}{2}, j\right) & \text{if } i = 2n \\ 0 & \text{otherwise} \end{cases} \tag{32}$$

where $n = 1, \ldots, 6$. Because the existence of the disturbances is inevitable in any actual system, an integral controller (Tajdari et al., 2020a, 2019) is used. It helps to eliminate the constant disturbances (Åström and Hägglund, 1995), such as uncertainties in dynamical parameters. Accordingly, the main control problem coming from equation (28) should be reformulated by considering integral states (z) of S (i.e., as many as the number of links), described as

Table 2. Dynamical features of the robot's components.

Component	Dimension (m)	Inertia (kg.m^2)	Mass (kg)	Quantity
l_i	0.404	$I_x = 0.0016$ $I_y = 0.0016$ $I_z = 0.000001$	0.08	6
u_i	0.11	$I_x = 0.000001$ $I_y = 0.000058$ $I_z = 0.000060$	0.04	6
End effector	Circle (R_{up} = 0.12)	$I_x = 0.003$ $I_y = 0.003$ $I_z = 0.006$	4	1
Base	Circle (R_{down} = 0.22)	$I_x = 0.027$ $I_y = 0.027$ $I_z = 0.054$	7	1

$$z(k+1) = z(k) + \Delta t \overline{C} e(k) \\ = z(k) + \overline{C} e(k) \tag{33}$$

where $\overline{C}$ consists of $\overline{c}_{i,j}$ denoted as follows

$$\overline{c}_{i,j} = \begin{cases} \Delta t & \text{if } i = n, \quad \text{and} \quad j = 2i-1 \\ 0 & \text{otherwise} \end{cases} \tag{34}$$

Therefore, the resulted dynamic error of the system which appears after adding the integral states can be written as

$$e(k+1) = Ae(k) + B(k)T(k) + d(k) \tag{35}$$

accordingly

$$e = \begin{bmatrix} \overline{e} \\ z \end{bmatrix}, \quad d = \begin{bmatrix} \overline{d} \\ --- \\ 0_{S\times 1} \end{bmatrix} \tag{36}$$

$$A = \begin{bmatrix} \overline{A} & | & 0_{H\times S} \\ -- & -- & --- \\ \overline{C} & | & I_{S\times S} \end{bmatrix}, \quad B = \begin{bmatrix} \overline{B} \\ --- \\ 0_{S\times F} \end{bmatrix} \tag{37}$$

$$C = \begin{bmatrix} \overline{C} & I_{S\times S} \end{bmatrix} \tag{38}$$

where H is the number of dynamic states and F is the number of inputs, that is, number of actuators. Now, a quadratic cost function over an infinite time horizon can be defined as below. It is defined to minimize all the states' error and the control inputs

$$\min J = \sum_{k=0}^{\infty} \left[e^T(k) Q e(k) + T^T(k) R T(k) \right] \tag{39}$$

where

$$Q = \omega_Q I_{3S\times 3S}, R = \omega_R I_{S\times S} \tag{40}$$

Matrices Q and R are weight matrices aiming to minimize all the states' error and the control signals. And the weighting matrices are formulated by $\omega_Q > 0$ and $\omega_R > 0$.

The resultant optimal control problem in equations (39) and (40) is solved by using a linear quadratic regulator (LQR). The goal is to stabilize feedback gains through the assumption (Tajdari and Roncoli, 2021), whereas stability and detectability criteria of Lewis et al. (2012) in chapter 2 should be satisfied by the original system in equation (35).

3.2. Stability and detectability

Stabilizability and detectability of the system in equation (35) are studied by conductin the Hautus test (Williams and Lawrence, 2007). Referring to Williams and Lawrence (2007), B is assumed to include more linearly independent columns in comparison with the number of unstable ($\lambda \leq 0$) modes, to be able to guarantee stability of the pair (A, B). Depending on the system topology, matrix $\overline{A}$ has the number of zero columns as many as links, which is cancelled with the columns of B and satisfies stabilizability criteria as

$$\text{rank}\left[(\lambda I - A) \quad B \right] = S + H \tag{41}$$

Now, the detectability of the system can be addressed in the pair $(A, C^T Q C)$; regarding Hespanha (2009), because $Q > 0$, this is essentially equal to study of the detectability of the pair (A, C). In the existing problem, the Hautus test condition is validated as follows in the situation that C contains at least one nonzero element in each column according to the marginally stable mode ($\lambda = 0$). By considering that, in all the discussed scenarios, the system is assumed to be observable

$$\text{rank}\begin{bmatrix} \lambda I - A \\ C \end{bmatrix} = S + H \tag{42}$$

3.3. Controller design and anti-windup

To solve the LQI problem, a linear feedback control law is proposed as follows

$$T(k) = -Ke(k) \tag{43}$$

where

$$K = \left(R + B^T P B \right)^{-1} B^T P A \tag{44}$$

$$P = C^T Q C + A^T P A - A^T P B \left(R + B^T P B \right)^{-1} \tag{45}$$

resulted K in equation (44) as optimal gain, and the algebraic Riccati equation equation (45) is investigated in Navvabi and Markazi (2019). Moreover, regarding practical implementation, the gain K is divided into two sections as follows

$$K = \begin{bmatrix} K_{\text{P}} & K_{\text{I}} \end{bmatrix} \tag{46}$$

which leads to reformulate the optimal control law as

$$T(k) = -K_{\text{P}} \overline{e}(k) - K_{\text{I}} z(k) \tag{47}$$

The final control law equation (47) is substantially effective for practical implementations because the computational effort manipulated by the feedback gains K_P and K_I presents considerably lower values.

In practical applications, achieving the exact values of the desired states may not be always possible due to uncertainties such as input saturation problem. Hence, it is prerequisite to use an anti-windup scheme within the proposed controller. The proposed scheme in Åström and Rundqwist (1989) is used in this study. In the case of this research, the scheme modifies the integral part of the dynamic controller equation (47) as

$$z(k+1) = (I + \Lambda K_{\mathrm{I}})z(k) + \left(\overline{C} + \Lambda K_{\mathrm{P}}\right)\overline{e}(k) + \Lambda \,\mathrm{sat}(T(k)) \tag{48}$$

where $\Lambda \in \mathbb{R}^{S\times F}$ and $(I + \Lambda K_{\mathrm{I}}) \in \mathbb{R}^{S\times S}$. Because the torque saturation is practically included on the real system input $T(k)$, the operator of the saturation is denoted as follows

$$\mathrm{sat}(T_o) = \begin{cases} T_o^{\min} & \text{if } T_o \le T_o^{\min} \\ T_o^{\max} & \text{if } T_o \ge T_o^{\max} \\ T_o, & \text{otherwise} \end{cases} \tag{49}$$

where o shows the corresponding index of each controlled input within the vector T, and $T_o^{\min}$ and $T_o^{\max}$ are the lower and upper borders, respectively, in regard to input T_o.

Therefore, the ultimate equations of the dynamic regulator are equations (47) and (48), which are practically effective and robust. Because it may affect the offline computation of the feedback gains K_{P}, K_{I}, in solving equations (44) and (45) (where B is time-varying), online calculations are restricted to solving equations (47) and (48).

It should be noted that while $T(k)$ does not exceed the saturation boundaries, the dynamics equation (48) is reduced to equation (33). Also, the numerical experiments clarify that the selection of different nominal values of T has explicitly no influence on the controller execution. It can be determined by the ability of the integral controller to dismiss the disturbances (Åström and Hägglund, 1995).

3.4. Anti-windup stability analysis in the closed-loop system

An essential constraint for the stability of the closed-loop system with the anti-windup scheme which conveys matrix Λ must be properly selected so that $I + \Lambda K_I$ has stable eigenvalues $\overline{\lambda}$ (Kapoor et al., 1998). This can be provided, for example, through classical pole placement or through a particular algorithm (look, e.g., Kapoor et al., 1998). Note the fact that while inputs are not saturated, the stability of the system is proved and ensured by the circumstances expressed in the Stability and detectability section. The section explains that the pair (A, B) and (A, C) are equivalent in the two cases; in addition, for the case that inputs are saturated, Λ must be opportunely designed, whereas it may influence the stability of equation (48).

To demonstrate the closed-loop system stability for the case that the inputs are saturated, equation (35) is reformulated as

$$e(k+1) = \overline{\overline{A}}e(k) + (B + R_{\mathrm{aw}}\Lambda)\mathrm{sat}(T(k)) \tag{50}$$

where

$$R_{\mathrm{aw}} = \begin{bmatrix} 0_{H\times H} \\ \hline I_{S\times S} \end{bmatrix}, \quad \overline{\overline{A}} = \left[\begin{array}{c|c} \overline{A} & 0_{H\times S} \\ \hline \left(\overline{C} + \overline{\Lambda} \overline{K_P}\right) & \left(\overline{I} + \overline{\Lambda} \overline{K_I}\right) \end{array}\right]. \tag{51}$$

Referring to da Silva Jr and Tarbouriech (2006), if a symmetric positive definite matrix is found as $W_{\mathrm{aw}} \in \mathbb{R}^{(H+S)\times(H+S)}$, a diagonal positive definite matrix is found as $S_{\mathrm{aw}} \in \mathbb{R}^{F\times F}$, and a matrix is found as $Z_{\mathrm{aw}} \in \mathbb{R}^{S\times F}$, subjects to

$$\Xi = \begin{bmatrix} W_{\mathrm{aw}} & -W_{\mathrm{aw}}K' & -W_{\mathrm{aw}}A' \\ -KW_{\mathrm{aw}} & 2S_{\mathrm{aw}} & SB' + Z'_{\mathrm{aw}}R'_{\mathrm{aw}} \\ -AW_{\mathrm{aw}} & BS_{\mathrm{aw}} + R_{\mathrm{aw}}Z_{\mathrm{aw}} & W_{\mathrm{aw}} \end{bmatrix} > 0 \tag{52}$$

Then, for $Z_{\mathrm{aw}} = \Lambda S_{\mathrm{aw}}$, the system in equation (50) is globally asymptotically stable. In this formulation, matrix W_{aw} can be defined as follows

$$W_{\mathrm{aw}} = \zeta I_{(H+S)\times(H+S)} \tag{53}$$

where ζ is a single parameter which should be properly computed. This investigation explains that by assessing circumstances of equation (52) for a satisfactory domain of $\overline{\lambda}$ and ζ, indicating the global asymptotic stability of the closed-loop system will be possible during optimizing controller parameters. This demonstrates the globally robustness of the closed-loop system in presence of disturbances and uncertainties as described in Khalil and Grizzle (2002).

3.5. Sensitivity analysis

To test the suggested strategy, the dynamic compensator equations (47) and (48) is applied to the nonlinear ADAMS model, whereas $\overline{\lambda}$ is considered as 0.5 for all the six stable poles of $I + \Lambda K_I$ in equation (48). First, a series of experiments are conducted to adjust the controller parameters. In the experiments with the time domain of 10 (s), the time step is considered as $\Delta t = 0.067$ (s) (it is same as the sample-rate frequency of the fabricated robot, 15 Hz, in the section of Experiment Setup). The desired values for ϕ, ψ, and θ are changing with peak-to-peak amplitude 30° and the frequency of 1 Hz, and the desired value of z is supposed to oscillate with peak-to-peak amplitude of 16 cm and the frequency of 1 Hz. Moreover, x and y desired values move periodically with frequency of 1 Hz and peak-to-peak amplitude of 8 cm.

Regarding investigating the sensitivity of the controller to select parameters w_Q, w_R, and $\overline{\lambda}$, we are using as assessment metric of the average percentage of final error. The

percentage of the final error E_p for each variable of the matrix $\overline{X}$ in equation (1) is explained as

$$\frac{E_{p_i} = \overline{X}_i^{t_{end}} - \overline{X}_{d_i}^{t_{end}}}{A_{m_i}} \times 100 \tag{54}$$

where $i = 1,\ldots, H/2, t_{end} = 10$ (s), and A_{m_i} denotes the peak-to-peak amplitude of the desired values $(\overline{X}_{d_i})$ of relative variable $(\overline{X}_i)$ (for the cases that the desired value is constant, A_{m_i} is considered as 1). Thus, the average percentage of final error $(\overline{E}_p)$ is formulated as

$$\overline{E}_p = \frac{2}{H}\sum_{i=1}^{H/2} E_{p_i} \tag{55}$$

Figure 3(a) shows how the achieved $\overline{E}_p$ differs by choosing fixed weights (as a pair) in the cost function equations (39) and (40). It can be inferred that the controller is able to obtain a low $\overline{E}_p$ value (blue areas) for an extensive range of the parameters. This demonstrates the controller is considerably impervious to the selection of the parameters. This is an advantage for real applications and explains less effort for tuning the control parameters to obtain satisfactory results.

Although the reasonable results (with acceptable $\overline{E}_p$ value) are achieved via numerical experiments, probably there are some cases (e.g., the saturation of several inputs) which might not occur in software simulations. These cases may lead the system to unstable conditions. Therefore, the stability of the closed-loop system is studied by the results extracted from the section of Anti-windup stability analysis in the closed-loop system. For instance, the fact that whether matrix Ξ in equation (52) is positive definite regarding an extensive range of $\overline{\lambda}$, and ζ is assessed. Concisely, the results for $\overline{\lambda} \equiv \overline{\lambda}_1 = \ldots = \overline{\lambda}_6$ are explicated in Figure 3(b), where it can be seen that no unstable eigenvalues exist for the domain of $0 \leq \overline{\lambda} \leq 1$. This implies that Ξ is positive definite. Consequently, it illustrates that allocating eigenvalues $\overline{\lambda}_1,\ldots,$ and $\overline{\lambda}_6$ within the range (0,1) produces proper results in terms of $\overline{E}_p$ (Figure 3(b)), and guarantees the asymptotic stability of the closed-loop system. Thus, $\overline{\lambda}$ is chosen as $\overline{\lambda} = 0.5$. According to Figure 3(b), at this point, the global stability of the system has the least sensitivity to changes of $\overline{\lambda}$.

Because the parameters of dynamic equations in equation (27) are time variants, $\overline{B}(k)$ is accordingly time variant. As a result, and based on equation (32), it is expressed that the error dynamic in equation (35) is nonlinear. Hence, it is logically expected that the system has different behavior in response to a different path. Therefore, nonlinearity of the system and the optimization method, and complexity of the problem, imply the use of intelligent methods (Ghaffari et al., 2018; Khodayari et al., 2015), which are capable to overcome the complexity and nonlinearity of the problem (Tarvirdizadeh et al., 2017; Tajdari et al., 2021b). Because of the fact that the cost function of the optimal problem in equation (39) is dependant on w_Q and w_R, obtaining a method to estimate the true values of w_Q and w_R in each time step is a key to solve the nonlinearities. Then, an innovative input–output ANN-based estimator is designed to estimate w_Q and w_R online. In the proposed methodology, as a common challenge in the intelligent methods, choosing appropriate inputs and outputs is substantially the most essential step. According to equation (39), w_Q defines the level of penalizing the states' error, and w_R optimizes the designed torques. Thus, state error functions and torque functions are suitable parameters as the estimator's inputs.

The functions are selected based on Tarvirdizadeh et al. (2018). Therefore, in this problem, density functions of error state and torques are appropriate functions to describe the changes, which are elaborated as follows

$$\rho_{\overline{e}}(k) = \Omega_{\overline{e}}(\overline{e}(k)) = \Re \frac{\overline{e}(k)}{\sum_{i=k-m}^{k} \overline{e}(i)} \tag{56}$$

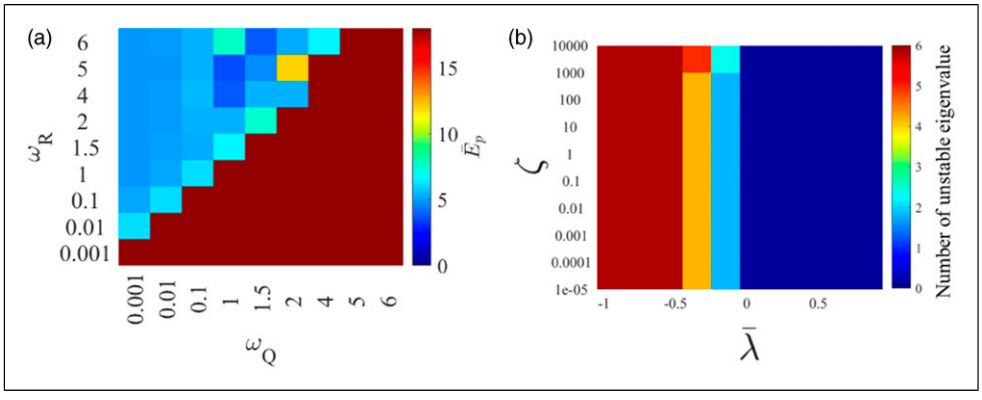

Figure 3. Numerical analysis. (a) Sensitivity analysis based on $\overline{E}_p$ for a domain of w_Q and w_R, where $\overline{\lambda} = 0.5$. (b) Number of negative eigenvalues in Ξ, where w_Q = 1, w_R = 4 for a domain of $\overline{\lambda}$ nad ζ. ANN estimator design for w_Q and w_R.

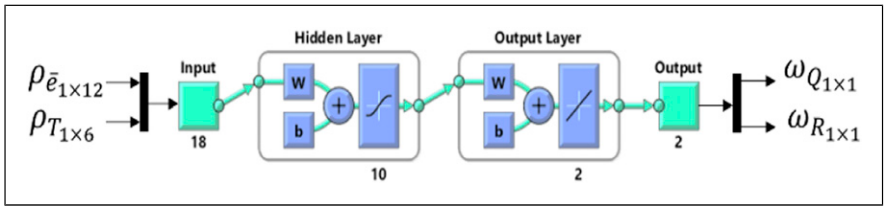

Figure 4. Designed artificial neural network estimator structure.

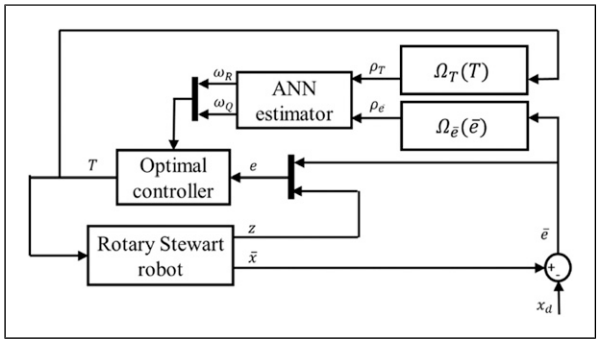

Figure 5. Closed-loop control diagram.

Table 3. Motor specifications.

Item	Specification
Motor	Coreless (Maxon)
Motor type	Rotary MX-64 DYNAMIXEL
Input voltage	10.0–14.8 (V) (recommended: 12.0 (V))
No load speed	58 (rev/min) (at 11.1 (V))
Resolution	4096 (pulse/rev)
Weight	165 (g)
Dimensions (W x H x D)	40.2 × 61.1 × 41 (mm)
Stall torque	5.5 (N.m) (At 11.1 (V), 3.9 (A))
Physical connection	RS485/TTL multidrop bus

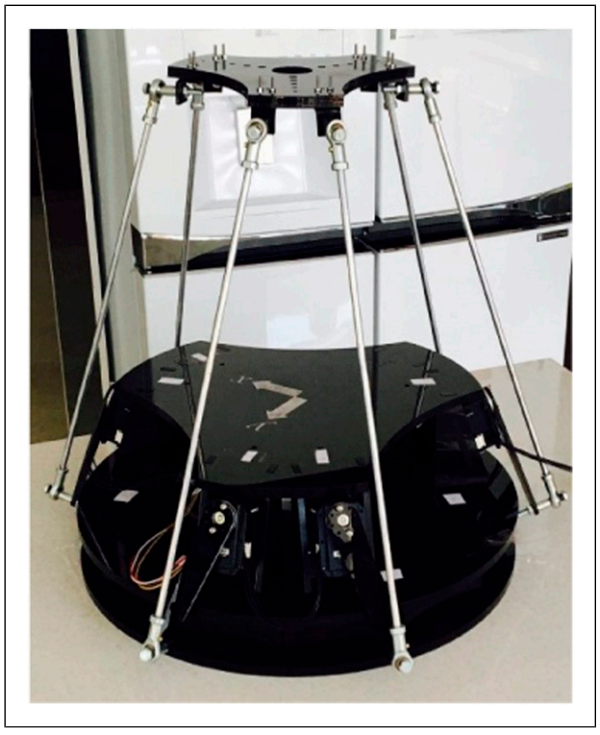

Figure 6. Fabricated rotary parallel robot.

$$\rho_T(k) = \Omega_T(T(k)) = \Re \frac{T(k)}{\sum_{i=k-m}^{k} T(i)} \tag{57}$$

where $\rho_{\bar{e}}$ is density of state errors and ρ_T is the torques' density. Actually, equations (56) and (57) are sensitive when $\bar{e}(k)$ and $T(k)$ are sufficiently greater than average of the variables with window size $\Re$. These criteria explain a smooth and logical stimulation to changes of the variables (Tarvirdizadeh et al., 2018). Consequently, the inputs of the intelligent estimator are $\rho_{\bar{e}_{1\times6}}$ and $\rho_{T_{1\times6}}$, and the outputs are $w_{Q_{1\times1}}$, and $w_{R_{1\times1}}$ as shown in Figure 4. According to the figure, there are 18 neurons in the input layer, 10 neurons in the hidden layer, and 2 neurons in the output layer. Also, activation function for the input and the output layers is linear and for the hidden layer is sigmoid. In addition, the training algorithm of the ANN is a Levenberg–Marquardt backpropagation method based on Kosko and Burgess (1998), Levenberg (1944), and Marquardt (1963). To design an ANN-based estimator, a set of data including the inputs–outputs is essential. Therefore, the controller of equation (47) is used as a master for the estimator. To collect data, the output of the controller in the stable regions (blue areas) of Figure 3(a) is used, whereas $\Re = 31$, $T_o^{\max} = 1.5$ N.m, and $T_o^{\min} = -1.5$ N.m. Going into detail, all the experiments of the figure where $w_R > w_Q$ and $0.001 < w_Q < 4$ are considered. To check the effects of the desired value frequency, the mentioned experiment is repeated with the frequencies of 0.5 Hz, 2 Hz, 4 Hz, and 6 Hz. Thus, the appropriate inputs–outputs of the estimator are generated with a sample number of 11,250.

To design the estimator, the dataset is randomly divided into two subsets: the training and the testing data subsets. The first data subset is used to develop and fine-tune the estimator. Afterward, the second data subset is used to assess the estimator performance, which does not affect the

training data subset. Thus, the first data subset, which contains 70% of the master dataset, is considered for training and the remaining of 30% is used to validate the obtained model. Figure 5 shows the closed-loop optimal feedback control diagram of the proposed system, where the ANN estimator based on the error states and the torques' values, updates the controller gains of w_Q and w_R in each time step.

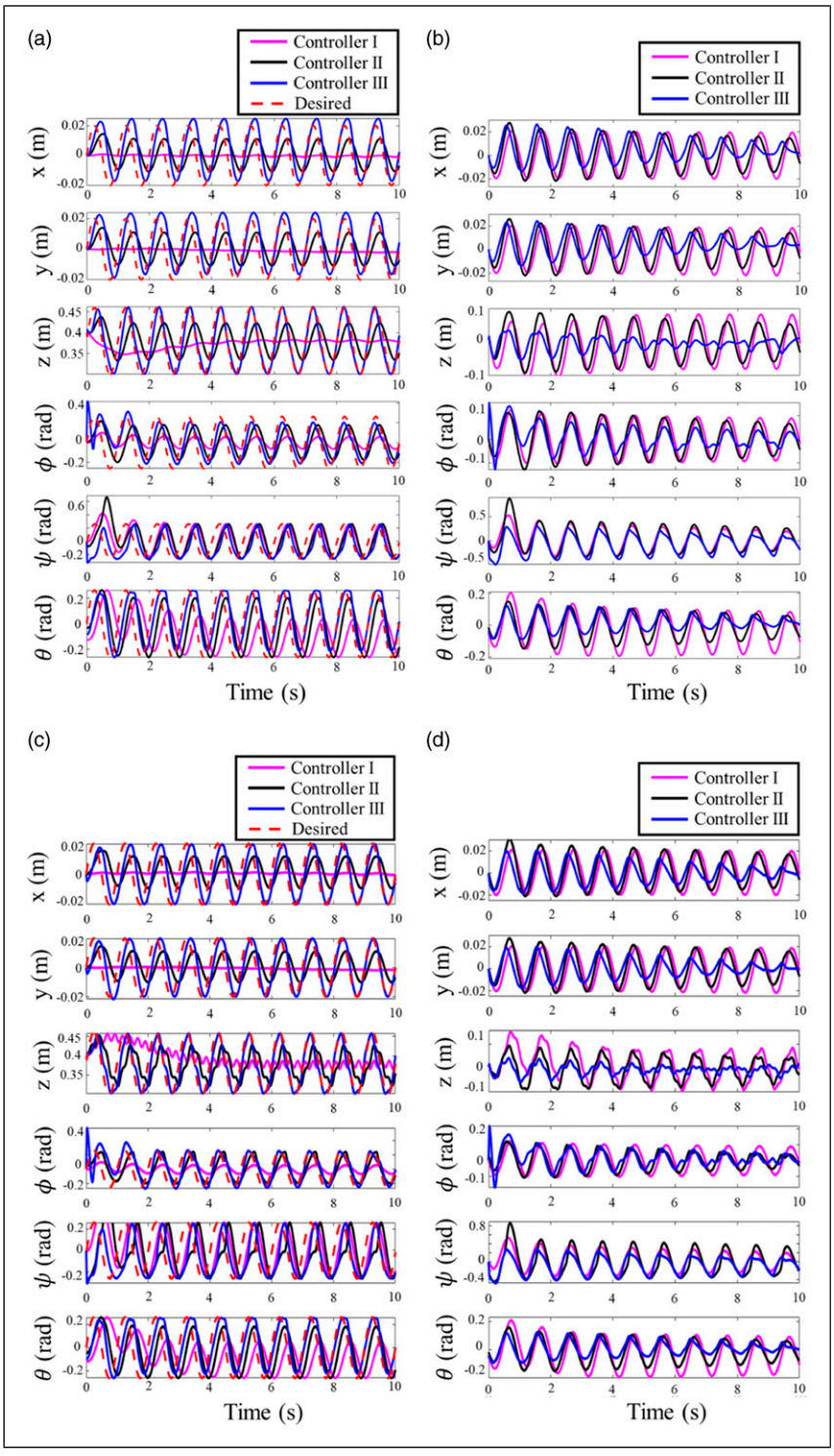

Figure 7. Controlled case performance through the ADAMS model. Main states $(\overline{X})$: (a) constant mass value of m = 4 kg and (c) time-varying mass value in equation (60). Error of Main states $(\overline{X} - \overline{X}_d)$: (b) constant mass value of m = 4 kg and (d) time-varying mass value in equation (60).

4. Experiment setup

To evaluate the controller in a real nonlinear system with natural disturbances, the introduced robot in Figure 2 was fabricated. As Figure 6 depicts, 6 servo motors of mx-64 are used as torque manipulators and are controlled directly with MATLAB through USB2Dynamixel (Robotis, (2019b). These motors are selected due to having incremental encoder and torque meter with acceptable resolution. Moreover, the stall torque for these motors is 5.5 N.m, which is relatively high. The specifications of the motor extracted from Robotis (2019a) are reported in Table 3. Moreover, to measure the end effector position and angles ($\overline{X}$), a 9-DOF absolute orientation IMU fusion breakout - BNO055 is used and data of the sensor are filtered and imported to MATLAB through an Arduino Mega 2560. The BNO055 sensor, which is located in the center of the end effector, spits out Euler angles and vectors as mentioned in Adafruit (2019). The frequency of the final product for sending and receiving data is averagely 15 Hz, which is obtained experimentally. Moreover, the saturation boundary value of the motors is set as 1.5 N.m according to safety and prevention of the motor damages.

5. Results

5.1. Simulation results

The simulation results are generated by implementing the proposed controller of equations (47) and (48) on the ADAMS model in Figure 2(c), where $\Re = 31$, $T_o^{\max} = 1.5$ N.m, and $T_o^{\min} = -1.5$ N.m. Also, the desired variables ($\overline{X}_d$) are considered as following

$$\overline{X}_d(t) = \begin{bmatrix} \phi_d(t) \\ \theta_d(t) \\ \psi_d(t) \\ x_d(t) \\ y_d(t) \\ z_d(t) \end{bmatrix} = \begin{bmatrix} \frac{\pi}{12}\mathrm{Sin}(t) \\ \frac{\pi}{12}\mathrm{Sin}(t) \\ \frac{\pi}{12}\mathrm{Sin}(t) \\ 0.02\,\mathrm{Sin}(t) \\ 0.02\,\mathrm{Sin}(t) \\ 0.08\,\mathrm{Sin}(t) + 0.38 \end{bmatrix} \quad (58)$$

where t is time. Considering Figure 7(a), the three control methodologies introduced in the Controller design section as: I. the controller without integral states, ANN estimator, and anti-windup; II. the anti-windup integral controller; and III. the anti-windup integral controller with ANN estimator, are investigated and compared. The anti-windup integral controller with the ANN estimator is applied to achieve perfect tracking (looking at Figure 7(a)) and reject the errors by the time as shown in Figure 7(b). The reduction of the error is concluded from the well-defined controller parameters, w_Q and w_R by the ANN estimator. The time-variant gains are reported in Figure 8(a), where they are always showing the stable area of Figure 3(a). However, the anti-windup integral controller without the estimator produces considerable errors, especially in the critical points of the desired path (i.e., the performances of the controller regarding the x, y, and z in Figure 7(b), showing the deviation, in spite of the fact that the controller tries to generate a similar periodic movement as the desired values). The final control scenario presents the implementation of a destined linear quadratic regulator (LQR) controller based on the dynamic error equation in equation (27). In this case, the controller with no integral states and no anti-windup scheme is designed. As shown in Figures 7(a) and (b), the controller fails completely regarding the x, y, and z states, and for the rest of the states, only a periodic movement with huge error is generated.

Moreover, the implemented torques (T_i in equation (16)) on the system for the three control scenarios are shown in Figure 9. Based on Figure 9(a), the controller I practically generates no control signals due to no tracking actions of the desired values in Figure 7(a). Comparing the torques in Figure 9(c) with Figure 9(e), the anti-windup integral controller with the ANN estimator offers less saturated (especially for the upper boundary saturation) and smaller torque values in comparison to the anti-windup integral controller without the estimator. It is due to less tracking error, and consequently less integral states' values, which

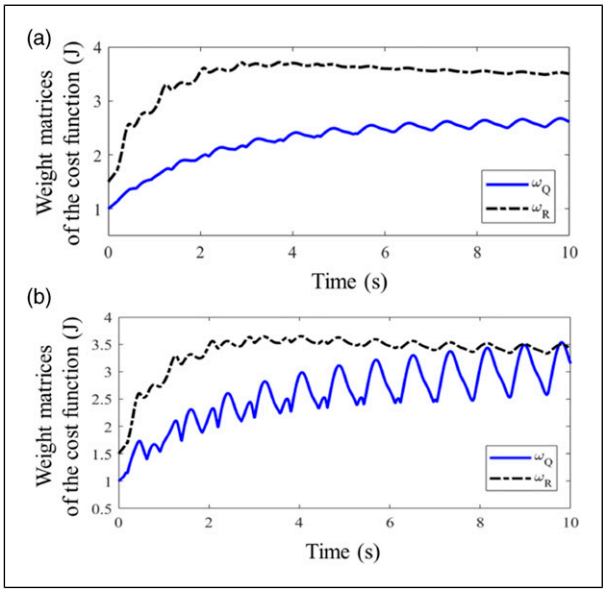

Figure 8. Online estimated of w_Q and w_R for the ADAMS model controlled case. (a) Constant mass value of m = 4 kg. (b) The time-varying mass value in equation (60).

are achieved by the anti-windup integral controller with the ANN estimator, rather than the integral controller without the estimator. Furthermore, the torque analysis is used to choose the electromotor discussed in the Experiment Setup section.

Envisioning the motor torque saturation, it is worth investigating the robustness of the controllers with respect to different kinds of constant and dynamic time-variant load torque with high probability of motor torque saturation. Accordingly, the effect is numerically studied through the following experiments.

Constant load torque investigation: Here, the experiment condition is exactly same as the previous experiments with an exception of the mass value (m). The value is changing in each experiment as m = 4, 5, 6, 7 and 8 kg. To compare the experiments in terms of the tracking error and the anti-windup scheme, two criteria of accumulative absolute percentage error E_{ac} and total saturation time are introduced as follows

$$E_{ac} = \frac{2}{H}\sum_{i=1}^{H/2}\int_0^t \left(\frac{\left|\overline{X}_i(t) - \overline{X}_{d_i}(t)\right|}{A_{m_i}} \times 100\right) dt \qquad (59)$$

where E_{ac} is the accumulative absolute percentage error and is denoted as the summation of the absolute percentage error in each time step. All the variables are introduced in equation (54). Then, the total saturation time which is called t_{sat} is the summation of all time intervals when each motor is saturated. In other words, the maximum value of the total saturation time will be 60 s (10 s for each motor), if the run time of the experiment is 10 s. Accordingly, the controllers' performances are individually reported based on the two criteria in Table 4. Based on the table, the E_{ac} for the

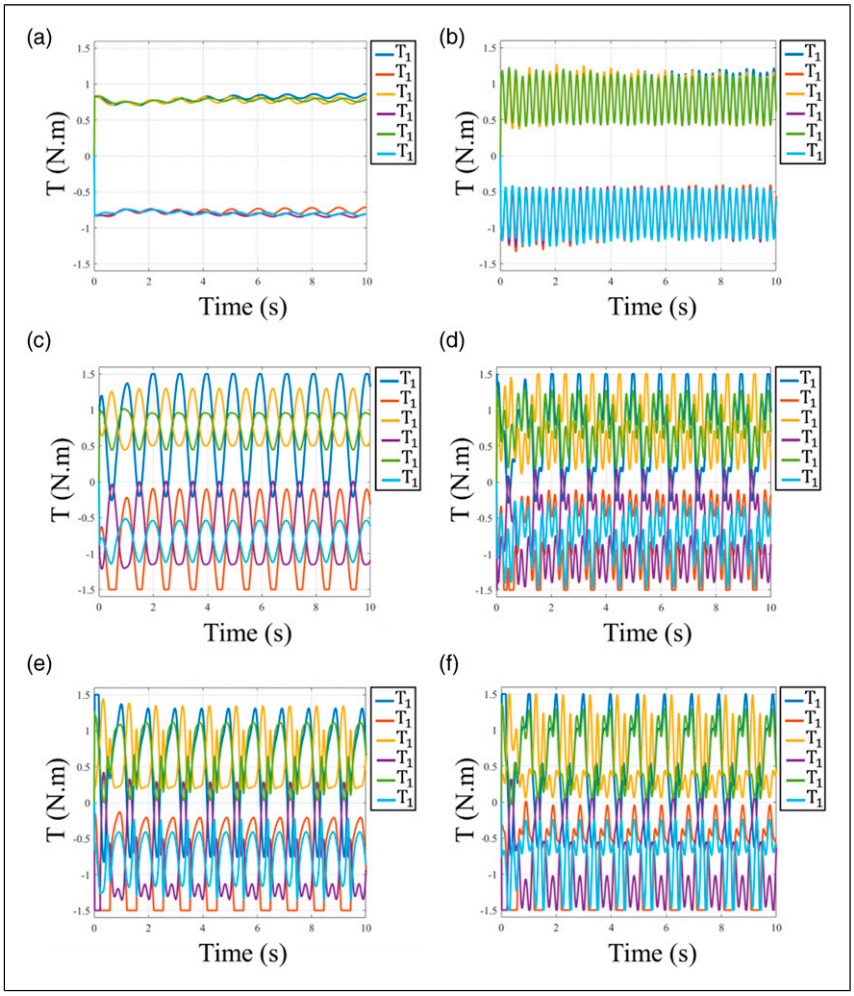

Figure 9. Motor torques for the ADAMS model controlled case. Controller I: (a) constant mass value of m = 4 kg and (b) time-varying mass value in equation (60). Controller II: (c) constant mass value of m = 4 kg and (d) time-varying mass value in equation (60). Controller III: (e) constant mass value of m = 4 kg and (f) time-varying mass value in equation (60).

controller I is increasing smoothly, and in comparison to the other two controllers, it is higher in the most cases. This is because the controller cannot track the desired values and mostly the end effector stays sedentary-like in the initial condition (e.g.,. Looking at the experiment in Figure 9(a), the generated torques by the controller I, tackle mainly the torque load and cannot follow the desired values). The constant-like torques also result in zero saturation time. Afterward, the controller II is using the anti-windup scheme with integral states. Thus, perfect tracking is expected; however, the degree of saturation is a restriction to the perfect tracking as the integral states grow up during saturation. It may result in more intensified reactions from the controller and then may lead into instability. As can be seen from the table, by increasing the m, the E_{ac} and the t_{sat} are increasing as expected. Even for the case $m = 8$ kg, the E_{ac} for the controller II is higher than the controller I, showing that the saturation time is the controller failure cause. Hence, the controller III performs with higher robustness rather than the controller II even in higher saturation time. It highlights the positive impact of adding the ANN estimator to tune the controller gains based on the errors. According to Table 4, it also demonstrates an improvement of 45% and 46% for the controller III, in terms of the E_{ac}, comparing to the controller II and the controller I, respectively.

Table 4. Accumulative absolute percentage error (E_{ac}) and the total saturation time report (t_{sat}).

	Controller I		Controller II		Controller III	
m (kg)	E_{ac}	t_{sat} (s)	E_{ac}	t_{sat} (s)	E_{ac}	t_{sat} (s)
4	219	0	213	3.8	111	6.2
5	221	0	214	4.0	112	9.0
6	223	0	214	6.2	114	10.4
7	224	0	217	7.6	120	13.6
8	225	0	229	10.8	143	18.8

Time-variant load torque investigation: Accordingly, an experiment is arranged where the mass of the end effector is time-varying as follows

$$m(t) = m_0(1 + 0.75\sin(2t)) \tag{60}$$

where $m_0 = 4$ kg, and the frequency of changes is in the trained data domain of the desired values, same as the section of ANN estimator design for w_Q and w_R, which is equal to 2 Hz. Accordingly, the tuned matrix on w_Q and w_R is depicted in Figure 8(b), which shows higher fluctuating graph for the gains in comparison with the constant mass in Figure 8(a). Comparing Figure 7(b) with Figure 7(d) in higher errors, the fluctuation is expected and is a reaction to mass variation. Also, one important point in this figure is that the w_Q is fluctuating with higher amplitude than w_R and the

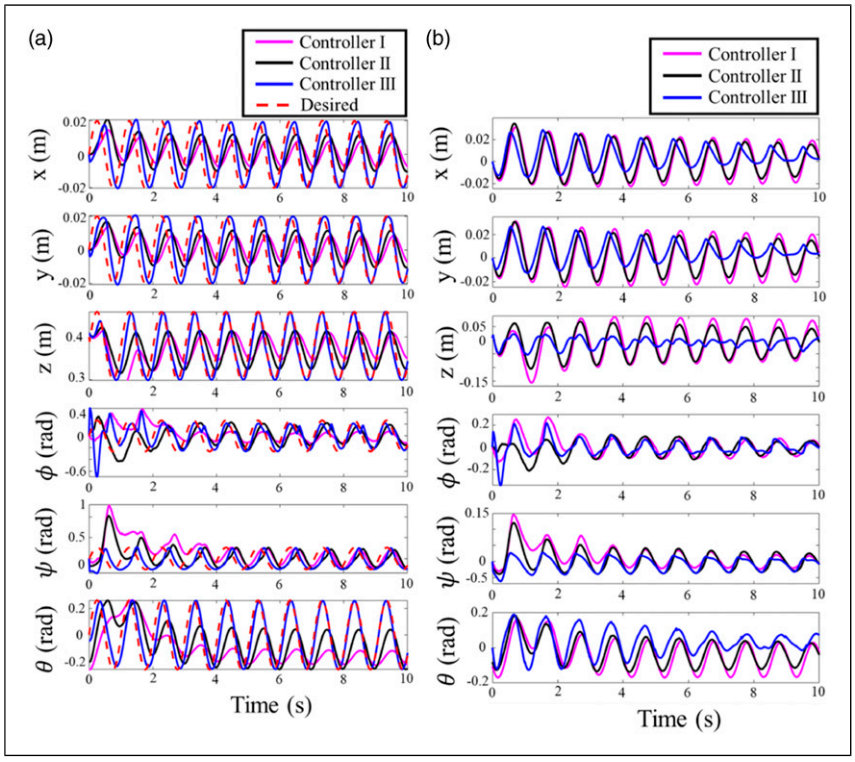

Figure 10. Controlled case performance through the fabricated robot. (a) Main states ($\overline{X}$). (b) Error of main states ($\overline{X} - \overline{X}_d$).

constant mass scenario. This is because the mass variation impacts the error states more easily (or the E_{ac}) in Figures 7(c) and (d) than the torques in Figures 9(b), (d), and (f), which leads into bigger integral state values. Thus, the fluctuation amplitude for w_Q should be higher than w_R because w_Q is responsible for penalizing state errors.

5.2. Experiment results

To validate and investigate the reliability of the proposed controller in the presence of real disturbances and uncertainties, the controller is implemented on the robot introduced in the Experiment Setup section. To have a comparison with the simulation output, the same desired values in equation (58) are used. All the other control parameters and initial conditions are considered the same as the Simulation results section. Performances of the controllers for the main states are depicted in Figure 10(a). Comparing the results of the three controllers in the figure gives the same conclusion as the previous section because the rate of the error rejection for the anti-windup integral controller with the ANN estimator (controller III) is considerably higher than the other two controllers. However, more overshoot is observed in the beginning of the test. The overshoot happened regarding the unexpected actuators' lag and unidentified dynamical parameters. This issue is also detectable in the trajectories of the estimated w_Q and w_R in Figure 11 as they have high fluctuating behavior in the beginning of the test, whereas they are converging by the time to specific values. In addition, the ANN estimator is supposed to present the parameters in which the tracking errors are minimized. Only for the control strategy with the estimator, the tracking errors drawn in Figure 10(b) are decreasing by the time due to w_Q and w_R identification. This infers well-practical performance of the estimator. Comparing the torque diagrams in Figure 12 illustrates that outputs of the controller with the ANN estimator (controller III) in Figure 12(c) are saturated in more time span comparing to Figures 12(a) and (b), although the results show zero-converging error for the controller. This implies a logic cooperation between the estimator and the anti-windup

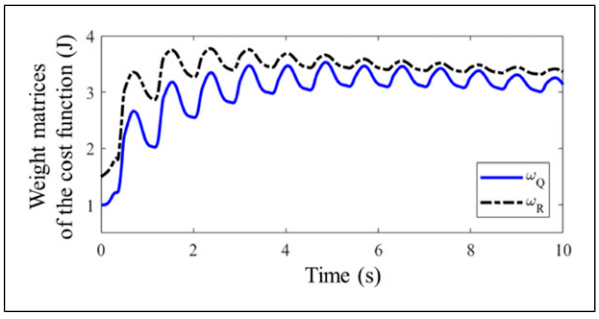

Figure 11. Online estimated of w_Q and w_R for the fabricated robot controlled case.

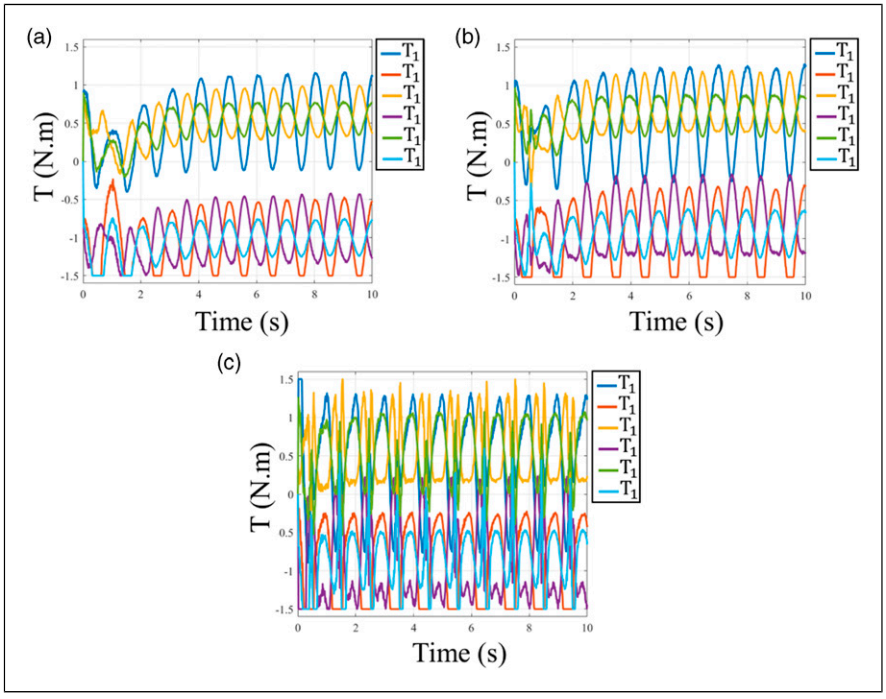

Figure 12. Motor torques for the fabricated robot controlled case. (a) Controller I. (b) Controller II. (c) Controller III.

scheme in equation (48), resulted from little sensitivity of the parameters choice to performance of the controller.

6. Conclusion

In this article, an innovative control methodology for a Stewart platform parallel robot with rotary actuators was investigated. The equations of motion for the system were derived and a 3D model of the system was also implemented in ADAMS. In addition, the analyses of the kinematic, dynamic, and control of the robot were investigated based on the obtained nonlinear model. To attain a desired amount of the end effector tracking error, the gain tuning LQI controller. The robustness and insensitivity of the parameter choices, besides the adaptive component, that is, the ANN estimator, made practical implementation easier, without the necessity of lengthy and costly measurements of the dynamic parameters. Finally, the simulation results revealed that the optimal LQI controller with intelligent estimator was able to control the dynamic of the system and eliminate the tracking error 45% more than the other compared controllers, averagely, considering the existence of the realistic dynamic forces and saturation in the ADAMS model. Also, the methodology was evaluated by the fabricated rotary Stewart robot to investigate the robustness of the controller with respect to the dynamic parameters, uncertainty, and realistic noise. Future developments include the optimal dimension design subject to the dynamic of the system and the study of the controller sensitivity regarding the dimension of the robot and dynamic parameters. In addition, the fabrication of a faster and smaller robot integrated with a time-delay optimal controller is another topic for the future studies to be easily adaptable to other practical cooperative robots.

Declaration of conflicting interests

The author(s) declared no potential conflicts of interest with respect to the research, authorship, and/or publication of this article.

Funding

The author(s) received no financial support for the research, authorship, and/or publication of this article.

ORCID iD

Farzam Tajdari https://orcid.org/0000-0001-7378-0368

References

Adafruit (2019) Adafruit 9-DOF absolute orientation IMU fusion breakout - BNO055. https://www.adafruit.com/product/2472

Åström KJ and Hägglund T (1995) *PID controllers: theory, design, and tuning*. NC: Instrument society of America Research Triangle Park, Vol. 2.

Åström KJ and Rundqwist L (1989) Integrator windup and how to avoid it. In: 1989 american control conference, Pittsburgh, PA, USA, 21–23 June 1989. New York, USA: IEEE.

Bingul Z and Karahan O (2012) *Dynamic Modeling and Simulation of Stewart Platform*. London, UK: INTECH Open Access Publisher.

Cafolla D and Marco C (2015) Design and simulation of humanoid spine. In: *New Trends in Mechanism and Machine Science*. Berlin, Germany: Springer, pp. 585–593..

Chen Z, Chen Y and Huang Q (2015) Development of a wireless and near real-time 3d ultrasound strain imaging system. *IEEE Transactions on Biomedical Circuits and Systems* 10(2): 394–403.

da Silva JMG Jr and Tarbouriech S (2006) Anti-windup design with guaranteed regions of stability for discrete-time linear systems. *Systems & Control Letters* 55(3): 184–192..

Dasgupta B and Mruthyunjaya TS (1998) A newton-euler formulation for the inverse dynamics of the stewart platform manipulator. *Mechanism and machine theory* 33(8): 1135–1152.

Do WQD and Yang DCH (1988) Inverse dynamic analysis and simulation of a platform type of robot. *Journal of Robotic Systems* 5(3): 209–227.

Fichter EF (1986) A Stewart platform- based manipulator: general theory and practical construction. *The International Journal of Robotics Research* 5(2): 157–182.

Furqan M, Suhaib M and Ahmad N (2017) Studies on stewart platform manipulator: a review. *Journal of Mechanical Science and Technology* 31(9): 4459–4470.

Geng Z, Haynes LS, Lee JD, et al. (1992) On the dynamic model and kinematic analysis of a class of stewart platforms. *Robotics and autonomous systems* 9(4): 237–254.

Ghaffari A, Khodayari A, Kamali A, et al. (2018) New fuzzy solution for determining anticipation and evaluation behavior during car-following maneuvers. *Proceedings of the Institution of Mechanical Engineers, Part D: Journal of automobile engineering* 232(7): 936–945.

Gough V (1957) Contribution to discussion of papers on research in automobile stability, control and tyre performance. *Proceedings of the Automobile Division Institution Mechanical Engineers* 171: 392–395.

Gough VE (1962). *Universal tyre test machine*. London: Proc. FISITA 9th Int. Technical Congr., 117–137.

Hespanha JP (2009) *Linear Systems Theory*. New Jersey, USA: Princeton University Press.

Hopkins BR and Williams RL (2002) Kinematics, design and control of the 6-PSU platform. *Industrial Robot: An International Journal* 29(5): 443–451.

Huang CI and Fu LC (2004) Adaptive backstepping tracking control of the stewart platform. In: 2004 43rd IEEE conference on decision and control (CDC), Nassau, Bahamas, 14–17 December 2004. New York, USA: IEEE Cat. No. 04CH37601) IEEE, Vol. 5, pp. 5228–5233.

Huang Q, Lan J and Li X (2018) Robotic arm based automatic ultrasound scanning for three-dimensional imaging. *IEEE Transactions on Industrial Informatics* 15(2): 1173–1182.

Huang Y, Pool DM, Stroosma O, et al. (2016) A review of control schemes for hydraulic stewart platform flight simulator motion systems. In: AIAA modeling and simulation technologies conference, San Diego, California, USA, 4–8 January 2016. San Diego, CA: AIAA, pp. 1436.

Kapoor N, Teel AR and Daoutidis P (1998) An anti-windup design for linear systems with input saturation. *Automatica* 34(5): 559–574.

Khalil HK and Grizzle JW (2002) *Nonlinear systems*. Upper Saddle River, NJ: Prentice-Hall, Vol. 3.

Khodayari A, et al. (2015) A new model of car following behavior based on lane change effects using anticipation and evaluation idea. *Iranian Journal of Mechanical Engineering Transactions of the ISME* 16(2): 26–38.

Kizir S and Bingul Z (2012). *Position control and trajectory tracking of the stewart platform. Serial and parallel robot manipulators-kinematics, dynamics, control and optimization*. Istanbul, Turkey: InTech. Chapters published under CC BY 3: 179–202.

Kosko B and Burgess JC (1998) Neural Networks and Fuzzy Systems. *Journal of the Acoustical Society of America* 103: 3131.

Kwon K and Kim C (2012) How to design personalization in a context of customer retention: Who personalizes what and to what extent? *Electronic Commerce Research and Applications* 11(2): 101–116.

Lebret G, Liu K and Lewis FL (1993) Dynamic analysis and control of a stewart platform manipulator. *Journal of Robotic systems* 10(5): 629–655.

Lee S-H, Song J-B, Choi W-C, et al. (2003) Position control of a stewart platform using inverse dynamics control with approximate dynamics. *Mechatronics* 13(6): 605–619.

Levenberg K (1944) A method for the solution of certain nonlinear problems in least squares. *Quarterly of applied mathematics* 2(2): 164–168.

Lewis FL, Vrabie D and Syrmos VL (2012) *Optimal Control*. New York, USA: John Wiley & Sons.

Lopes AM (2009) Dynamic modeling of a stewart platform using the generalized momentum approach. *Communications in Nonlinear Science and Numerical Simulation* 14(8): 3389–3401.

Marquardt DW (1963) An algorithm for least-squares estimation of nonlinear parameters. *Journal of the society for Industrial and Applied Mathematics* 11(2): 431–441.

Merlet J-P (1990) Force-feedback control of parallel kinematics manipulators. In: *Kinematic and Dynamic Issues in Sensor Based Control*. Berlin, Germany: Springer, pp. 143–158.

Merlet JP (2006) *Parallel robots*. Berlin, Germany: Springer Science & Business Media, Vol. 128.

Merouche S, Allard L, Montagnon E, et al. (2015) A robotic ultrasound scanner for automatic vessel tracking and three-dimensional reconstruction of b-mode images. *IEEE transactions on ultrasonics, ferroelectrics, and frequency control* 63(1): 35–46.

Navva`bi H and Markazi AHD (2019) New afsmc method for nonlinear system with state-dependent uncertainty: application to hexapod robot position control. *Journal of Intelligent & Robotic Systems* 95(1): 61–75.

Nomura K, Yonezawa T, Yonezawa T, et al. (2016) Development of six-dof human ankle motion control device using stewart platform structure for fall prevention. *Journal of Robotics and Mechatronics* 28(5): 654–663.

Orekhov AL, Black CB, Till J, et al. (2016) Analysis and validation of a teleoperated surgical parallel continuum manipulator. *IEEE Robotics and Automation Letters* 1(2): 828–835.

Patel V, Krishnan S, Goncalves A, et al. (2018) Sprk: a low-cost stewart platform for motion study in surgical robotics. In: International symposium on medical robotics (ISMR). Atlanta, GA, USA, 1–3 March 2018. New York, USA: IEEE, pp. 1–6.

Petrescu RV, Aversa R, Apicella A, et al. (2018) Inverse kinematics of a stewart platform. *Journal of Mechatronics and Robotics* 2(1): 45–59.

Robotis (2019a) *Mx - 64 Servo motor*. Available at: http://emanual.robotis.com/docs/en/dxl/mx/mx-64-2/

Robotis (2019b) *USB2Dynamixel*. Available at: http://emanual.robotis.com/docs/en/parts/interface/usb2dynamixel/

Shoham M, Burman M, Zehavi E, et al. (2003) Bone-mounted miniature robot for surgical procedures: concept and clinical applications. *IEEE Transactions on Robotics and Automation* 19(5): 893–901.

Sosa-Méndez D, Lugo-González E, Arias-Montiel M, et al. (2017) ADAMS-MATLAB co-simulation for kinematics, dynamics, and control of the Stewart–Gough platform. *International Journal of Advanced Robotic Systems* 14(4): 1–10.

Stewart D (1965) A platform with six degrees of freedom. *Proceedings of the institution of mechanical engineers* 180(1): 371–386.

Sugimoto K (1989) Computational scheme for dynamic analysis of parallel manipulators. *Journal of mechanisms, transmissions, and automation in design* 111(1): 29–33.

Sun Y, Jiang Z, Qi X, et al. (2018) Robot-assisted decompressive laminectomy planning based on 3d medical image. *IEEE Access* 6: 22557–22569.

Taghirad HD (2013) *Parallel Robots: Mechanics and Control*. USA: CRC Press.

Tajdari F, Kabganian M, Khodabakhshi E, et al. (2017a) Design, implementation and control of a two-link fully-actuated robot capable of online identification of unknown dynamical parameters using adaptive sliding mode controller. In: artificial intelligence and robotics (IRANOPEN), Qazvin, Iran, 9 April 2017. New York, USA: IEEE, pp. 91–96.

Tajdari F, Kabganian M, Rad NF, et al. (2017b) Robust control of a 3-dof parallel cable robot using an adaptive neuro-fuzzy inference system. In: 2017 artificial intelligence and robotics (IRANOPEN), Qazvin, Iran, 9 April 2017. New York, USA: IEEE, pp. 97–101.

Tajdari F and Roncoli C (2021) Adaptive traffic control at motorway bottlenecks with time-varying fundamental diagram. In: CTS2021: 16th IFAC symposium on control in transportation systems, Lille, France, June 2021. Amesterdam, Netherlands: Elsevier.

Tajdari F, Roncoli C, Bekiaris-Liberis N, et al. (2019) Integrated ramp metering and lane-changing feedback control at motorway bottlenecks. In: 2019 18th European control conference (ECC), Naples, Italy, 25–28 June 2019. New York, USA: IEEE, pp. 3179–3184.

Tajdari F, Roncoli C and Papageorgiou M (2020a) Feedback-based ramp metering and lane-changing control with connected and automated vehicles. *IEEE Transactions on Intelligent Transportation Systems* 99: 1–13.

Tajdari F, Tajdari M and Rezaei A (2021a) Discrete time delay feedback control of stewart platform with intelligent optimizer weight tuner. In: 2021 IEEE international conference on robotics and automation (ICRA), IEEE. In Press.

Tajdari F, Toulkani NE and Zhilakzadeh N (2020b) Intelligent optimal feed-back torque control of a 6dof surgical rotary robot. In: 2020 11th power electronics, drive systems, and technologies conference (PEDSTC). Tehran, Iran, 4–6 February 2020. New York, USA: IEEE, pp. 1–6.

Tajdari F, Toulkani NE and Zhilakzadeh N (2020c) Semi-real evaluation, and adaptive control of a 6dof surgical robot. In: 2020 11th power electronics, drive systems, and technologies conference (PEDSTC). Tehran, Iran, 4–6 February 2020. New York, USA: IEEE, pp. 1–6.

Tajdari M, Pawar A, Li H, et al. (2021b) Image-based modelling for adolescent idiopathic scoliosis: mechanistic machine learning analysis and prediction. *Computer methods in applied mechanics and engineering* 374: 113590.

Tarvirdizadeh B, Golgouneh A, Khodabakhshi E, et al. (2017) An assessment of a similarity between the right and left hand photoplethysmography signals, using time and frequency features of heart-rate-variability signal. In: IEEE 4th international conference on knowledge-based engineering and innovation (KBEI). Tehran, Iran, 22 December 2017, New York, USA: IEEE.

Tarvirdizadeh B, Golgouneh A, Tajdari F, et al. (2018) A novel online method for identifying motion artifact and photoplethysmography signal reconstruction using artificial neural networks and adaptive neuro-fuzzy inference system. *Neural Computing and Applications* 32: 1–18.

Tourajizadeh H, Yousefzadeh M and Tajik A (2016) Closed loop optimal control of a stewart platform using an optimal feedback linearization method. *International Journal of Advanced Robotic Systems* 13(3): 134.

Van Nguyen T and Ha C (2018) Rbf neural network adaptive sliding mode control of rotary stewart platform. In: International conference on intelligent computing methodologies, Wuhan, China, 15–18 August 2018, Berlin, Germany: Springer, pp. 149–162.

Williams RL, Lawrence DA, et al. (2007) *Linear State-Space Control Systems*. London, UK: Wiley Online Library.

Yang X, Wu H, Chen B, et al. (2019) Dynamic modeling and decoupled control of a flexible stewart platform for vibration isolation. *Journal of Sound and Vibration* 439: 398–412.

Yang Y, Yuan T, Huysmans T, et al. (2020) Posture-invariant 3d human hand statistical shape model. *Journal of Computing and Information Science in Engineering* 21: 1–31.